



Oscillations of a layer of viscoelastic fluid under steady forcing

Bin Liu^{a,*}, Michael Shelley^a, Jun Zhang^{a,b}

^a Applied Mathematics Laboratory, Courant Institute of Mathematical Sciences, New York University, 251 Mercer Street, New York, NY 10012, USA

^b Department of Physics, New York University, 4 Washington Place, New York, NY 10003, USA

ARTICLE INFO

Article history:

Received 2 December 2011

Received in revised form 29 February 2012

Accepted 8 March 2012

Available online 17 March 2012

Keywords:

Viscoelastic

Low Reynolds number mixing

Turbulence

ABSTRACT

We study the dynamics of a layer of viscoelastic fluid, in the Stokesian regime, that is driven from below by a 4×4 checkerboard pattern of rotating and counter-rotating disks. At low disk rotation rate (low Weissenberg number) the fluid flow response is slaved to the geometry of this forcing and divides into many steadily rotating cells, each contained within invariant manifolds issuing from hyperbolic stagnation points. As the rotation rate increases these fluid cells begin to oscillate periodically in a synchronized fashion. At a yet higher rotation rate, this temporally periodic flow disappears and is replaced by a richer, “turbulent” dynamics where the flow is delocalized from the forcing and has fluid cells that are continuously destroyed and reformed.

Published by Elsevier B.V.

1. Introduction

Newtonian fluids in the low Reynolds number limit (i.e. Stokesian) have a linear response to external forcing, and can only display steady flow in response to steady forcing. Hence, a Stokesian Newtonian fluid cannot develop any intrinsic dynamics or flow instabilities as would be associated with turbulence at high Reynolds number. Turbulent flow is associated with the convective terms in the Navier–Stokes equations which introduce nonlinearity and destroy the reversibility of the Stokesian case. Simple models of viscoelastic polymer solutions, such as the Oldroyd-B or FENE models [1], show that viscoelasticity reintroduces convective nonlinearity through polymer stress transport, even in the Stokesian case, and that the storage and release of elastic stress destroys flow reversibility. Thus, the possibility of having rich dynamics despite the absence of fluid inertia motivated experimental studies of the response of viscoelastic fluids to rotational shear or to flow through wavy channels [2,3]. These studies showed that even at low Reynolds numbers viscoelastic fluids can exhibit some aspects of turbulence such as unpredictability and convective fluid mixing (see [1] for related earlier work on nonlinearity and flow unsteadiness).

Viscoelastic fluids in a laboratory setting are typically composed of Newtonian solvents containing a suspension of polymers. These polymers can be stretched and reoriented, particularly by extensional flows near hyperbolic stagnation points [4], and can display stretch-coil transitions [5,6]. Likely related to this are observations of symmetry breaking and spontaneous oscillation of viscoelastic fluids in micro-fluidic channels [7–9]. Simulations of a viscoelastic

fluid under a “four-roll-mill” forcing show transitions to flow asymmetry, followed by transition to a complex dynamics with multiple frequencies of oscillation, coherent structures, and fluid mixing [10,11]. Similar transitions to temporal oscillating states has been observed in a two-dimensional Kolmogorov flow geometry [12].

Here, in an experimental study most closely related to the theoretical studies of Thomases et al. [10,11], we consider the dynamics of a viscoelastic fluid evolving over a checker-board array of rotating and counter-rotating disks. We find that at low to moderate rotation rates the flow transits from being an array of steadily rotating fluid cells to a set of oscillating, synchronized cells with a complex temporal phase arrangement. At yet higher rotating rate this synchronized state is destroyed and is replaced by a turbulent roiling dynamics with flow patterns delocalized from the regular forcing background.

2. Experimental setup

In our experiment, the forcing lattice is composed of 4×4 identical rotating disks (Fig. 1) and the lattice spacing is fixed at 19.1 mm. Two sets of disks with different radius r (3.2 mm and 6.4 mm) are used in the experiment, with the separations between adjacent disks L being 12.7 mm and 6.4 mm respectively. Each disk is driven by a rotary shaft that is kept vertical by a pair of embedded ball bearings. Each shaft is coupled to their immediate neighbor by spur gears, and all driven together by one stepper motor. In this way, all the disks rotate at the same frequency f (as the stepper motor), and any pair of adjacent disks rotate in opposite directions. Over the rotating disks lays a 1 cm thick layer of fluid. The Reynolds number is defined as $Re = \rho f r^2 / \eta$, where ρ is the fluid density

* Corresponding author.

E-mail address: binliu@cims.nyu.edu (B. Liu).

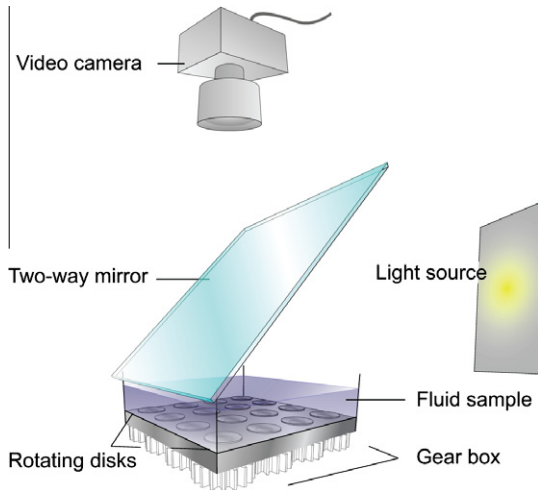


Fig. 1. Experimental setup. A layer of fluid is driven from below by a 4×4 array of rotating disks. The fluid is illuminated from above using a two-way mirror through which a top view of the flow pattern is also captured by an overhead high speed camera.

and η the shear-viscosity of the fluid. The viscoelastic fluids we use here are typical Boger fluids [13], which are elastic but with nearly constant shear-viscosity. In our experiment, Re never exceeds 0.3, so that the inertia of fluid is negligible. The viscoelasticity of the fluid is characterized by a dimensionless Weissenberg number, $Wi = \dot{\gamma}\tau$, where $\dot{\gamma}$ is the characteristic shear-rate of the flow, and τ is the relaxation time of the fluid.

Bulk flow patterns and stresses can be partially characterized by the surface morphology. The free surface bulges upwards where the internal stress is compressive (e.g., near the hyperbolic stagnation points in the Newtonian case), and downwards where the internal stress is extensive (e.g., at the center of Newtonian flow eddies). Surface morphology can be revealed by capturing the reflection of a diffusive light source, stronger in the center but gradually weaker toward the edges, shining from above (see Fig. 1). In our set-up, a high-speed video camera captures light reflected at nearly zero angle-of-reflection where a spatial overlap between the camera view and the light source is accomplished by using a two-way mirror oriented 45° away from the horizontal. The inclination of the fluid surface is shown by the intensity of reflected light: the darker the image, the more inclined the free surface, and vice versa. The ambiguity between a valley and a peak of the surface (both have strong reflection) can be resolved by any side-view of the fluid surface.

We find that at low to moderate rotation rates the driven fluid flow is close to being two-dimensional, though it is in fact weakly three-dimensional due to the forcing geometry. To characterize the nature of the flow field, we use the typical resident time of tracer particles (~ 0.05 mm in size) that appear within the illumination sheet. From this time scale t_{res} and the thickness of the light sheet d (~ 0.55 mm), we obtain a typical speed in the vertical direction $w = d/t_{res}$. The dimensionless ratio of the surface flow speed [$U = (v^2 + u^2)^{1/2}$] to the vertical speed, $Q = U/w$, serves as a rough indicator of the two-dimensional quality of the flow field. We refer to the quantity Q as the “2D-quality factor.”

In each flow setting (at given fluid viscosity and Wi), at least three tracer particles were used to compute the resident time t_{res} and consequently the 2D-quality factor Q . The particles are selected at different distances from the center of rotating disks, so that our characterization is not location specific. When the rotation frequency of the disks is low ($f = 2$ Hz) or when the free fluid surface deformation is small, we find that Q is large, typically around

200. For a Stokesian Newtonian fluid, the amount of surface deformation is determined by the competition between spatial stress due to viscosity, $\sim \eta f$, and gravity, $\sim \rho gh$ (where ρ is the fluid density, g the acceleration due to gravity, and h the fluid depth). Therefore, the greater the ratio $\rho gh/(\eta f)$, the greater the 2D-quality factor Q .

In the viscoelastic case (with $\eta \sim 1$ Pa s) and at moderate Weissenberg number (e.g., $Wi = 1.28$), we find $Q \sim 54$. At higher Weissenberg number (e.g., $Wi = 8.42$), Q decreases to around 18. More specifically, in the Newtonian case, we observe that tracer particles spiral inwards toward the axis of the disk – above which one finds the trough of the free surface – indicating a secondary flow that moves downward. Similarly, in the viscoelastic case we find that a secondary flow moves up near the disk’s center. Since factor Q is always greater than 18, the secondary flow velocity in the vertical direction never exceeds 6% of the horizontal flow velocities.

3. Observations

As a first test we introduce a Newtonian fluid, here a layer of 99% glycerol of depth $h \sim 1$ cm. The fluid layer displays a steady flow pattern when driven by the steadily rotating disks. The flow develops and saturates almost immediately (within 10 ms) with onset of disk rotation. As shown in Fig. 2a, there is a vortex sitting above each disk, with the set aligning perfectly with the forcing lattice. The free surface is depressed above each disk, marking the low pressure centers of the rotating fluid. The fluid eddies meet at relatively high ridges. The flow pattern is stable during the experiment. Once the disks cease rotation, the free surface relaxes almost immediately.

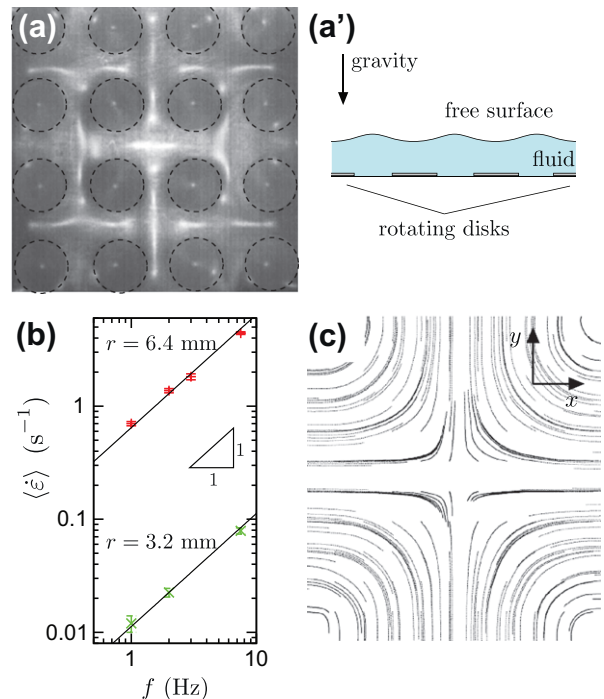


Fig. 2. Surface morphology and flow pattern of a Newtonian fluid above the 4×4 array of rotating disks. (a) Rotating fluid “cells”, seen as dark circles in the surface reflection, result from disk rotation. These cells have depressed centers above each rotating disk, as illustrated in a side-view schematic (a’). (b) The spatially averaged strain rate $\langle \dot{\epsilon} \rangle$ near the free surface as a function of disk rotation frequency. Two sets of rotating disks of different sizes ($r = 3.2$ mm and $r = 6.4$ mm) are used with fixed distance between adjacent disk centers ($L = 19.1$ mm). The depth of the fluid h is fixed at 11 mm. The solid lines are linear fits to the experimental data. (c) An example of the flow pattern at an extensional stagnation point as represented by the streamlines (curves).

With disk rotation the resultant flow depends upon disk size and their rotation rate. Other geometric factors, such as the ratios L/r and h/r , also play roles. Despite the presence of device boundaries, the flow pattern can be well-described as an array of vortices and extensional stagnation points. The extensional strain rates near the free surface, defined as $\dot{\epsilon} = \frac{1}{2} \left| \frac{\partial v}{\partial y} - \frac{\partial u}{\partial x} \right|$, are obtained by Particle Image Velocimetry (PIV) measurement. Here, u and v are the two components of fluid velocity \vec{V} along directions \hat{x} and \hat{y} , respectively. The flow is time-independent in the Newtonian, low-Re case with the strain rate depending on the intensity and geometry of the forcing. The flow pattern is invariant, despite varying the strain rate, if the same geometric factors are maintained. As shown in Fig. 2b, the mean strain rate $\langle \dot{\epsilon} \rangle$ (spatially averaged over the middle four fluid cells) is linearly proportional to the rotation frequency f for a given size of the rotating disks. This demonstrates that the fluid inertia is negligible within our tested regimes. The strain rate is sensitive to the geometric factors. By varying the rotation frequency and disk size r (with the geometric factors L/r and h/r varying accordingly), we can adjust the mean strain rate $\langle \dot{\epsilon} \rangle$ by a factor of two decades (from 0.1 s^{-1} to 10 s^{-1}). A typical flow pattern, from the PIV measurement, at a hyperbolic stagnation point is shown in Fig. 2c.

We now examine how a viscoelastic fluid responds to such forcing. An oft-used viscoelastic fluid is a dilute suspension of long-chain polymers – Polyacrylamide (PAA) of 1.8×10^7 in molecular weight (MW) – suspended in a 97% glycerol solution [14,7,9]. Here two different concentrations of polymers are used: $c = 40$ and 200 ppm. The viscoelasticity of these two fluids is characterized using a TA Instrument AR2000 Rheometer at room temperature ($T = 20 \text{ }^\circ\text{C}$). These fluids are typical Boger fluids [13], even though they slightly shear-thin. For polymer concentration of 40 ppm, its viscosity ranges from 0.88 (at 1 s^{-1}) to 0.79 Pa s (at 100 s^{-1}), with its mean $\eta = 0.82 \text{ Pa s}$. For 200 ppm solutions, the viscosity ranges from 2.17 (1 s^{-1}) to 1.28 Pa s (100 s^{-1}), with its mean $\eta = 1.48 \text{ Pa s}$. A Boger fluid is often described by the Oldroyd-B model [15,16], and from this the relaxation times of the fluids τ can be estimated from the first normal stress difference coefficient Ψ as $\tau = \Psi / [2(\eta - \eta_s)]$ [16], where η_s is the viscosity of the Newtonian solvent, i.e., the 97% glycerol solution with $\eta_s = 0.76 \text{ Pa s}$. The coefficients Ψ are obtained by the mean of the first normal stress difference coefficient when the shear rate is between 1 s^{-1} and 10 s^{-1} , where they vary significantly less than at higher shear rates. These coefficients Ψ are measured to be 0.054 Pa s^2 for $c = 40 \text{ ppm}$ and 3.9 Pa s^2 for $c = 200 \text{ ppm}$, which give the approximate relaxation times of $\tau = 0.48 \text{ s}$ and $\tau = 2.7 \text{ s}$, respectively.

Since we expect that polymer stretching will be driven primarily by flows at extensional stagnation points, we define a dimensionless Weissenberg number as $Wi = \dot{\epsilon}_c \tau$, where $\dot{\epsilon}_c$ is $\langle \dot{\epsilon} \rangle$ calculated from measurement of the Newtonian fluid under identical forcing (as used in [10]). The Weissenberg number characterizes how fast the flow is driven relative to its relaxation time, and is increased either by increasing the external forcing rate or by increasing the polymer concentration (which increases the relaxation time τ).

With the onset of disk rotation, the free surface of the viscoelastic fluid is divided into cells initially aligned with the square lattice, as shown in Fig. 3a, as is similar to the Newtonian case. Unlike the Newtonian case, the fluid cells quickly bulge upwards, becoming dome-like structures with convex top surfaces (shown in Fig. 3a'). This observation of upwards bulging is reminiscent of the well-known rod-climbing effect [17,18], and corresponds to the temporal development of non-Newtonian stresses within the bulk.

The fluid cells evolve in time and it takes about 10 s (somewhat longer but on the order of τ) before the internal polymer stress becomes fully developed (Fig. 3b). If the disks are halted the flow re-

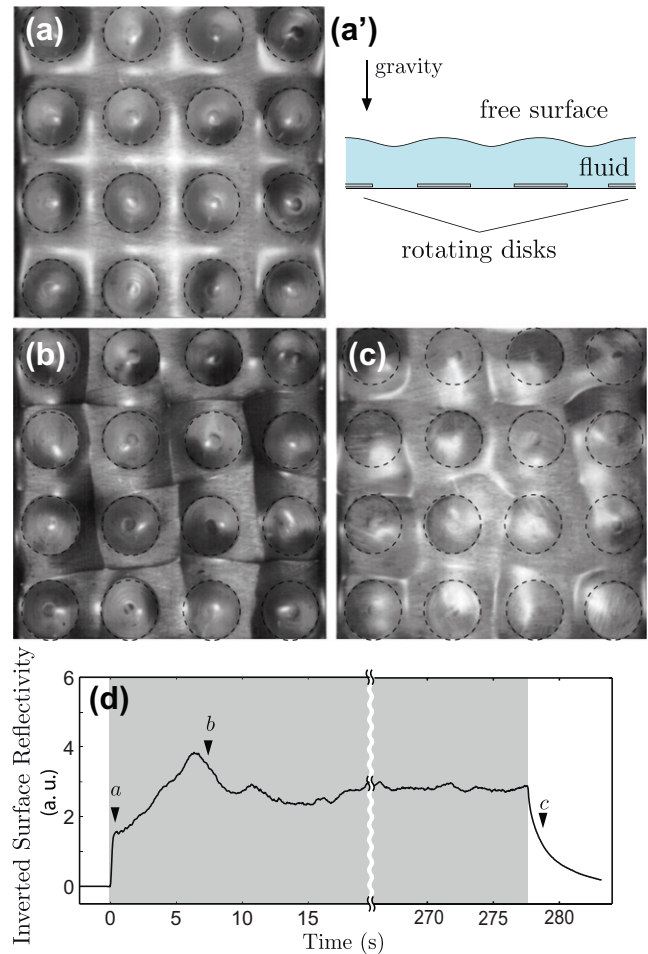


Fig. 3. Surface morphology and flow patterns of a viscoelastic fluid (200 ppm PAA in 97% glycerol) above the rotating disk array, with Weissenberg number $Wi = 4.9$. (a) The fluid initially forms a square lattice. The free surface of the fluid develops an inverted geometry [illustrated by a side-view (a')] as compared to the Newtonian case, within a small time interval ($t < 0.5 \text{ s}$). (b) As polymer stress builds, the fluid cells evolve and become misaligned relative to the forcing lattice. (c) When the disks stop rotating, the cells do not relax instantly, but are instead sustained by the residual stress for a few seconds. (d) The surface reflectivity averaged over the entire lattice as a function of time. The stages shown in (a), (b), and (c) are indicated by the annotated arrows.

laxes and the free surface flattens out. This time-scale reveals the fluid viscoelasticity, and provides an estimate of the fluid relaxation time (Fig. 3c). To do this, we use the reflectivity of the fluid surface to quantify the flatness of the free surface (a flat surface appears bright whereas an inclined surface will appear dark). As suggested in Fig. 3d, the relaxation of the mean surface inclination, which is roughly the inverted surface reflectivity, can be fitted by a decaying exponential. The decay rate β estimates the inverse of the fluid relaxation time τ . For a suspension of 200 ppm PAA, the decay (or relaxation) rate $\beta = 0.42 \pm 0.06 \text{ s}^{-1}$, which gives a time-scale $\tau \sim 1/0.42 = 2.4 \text{ s}$ and is consistent with the rheology measurement ($\tau = 2.7 \text{ s}$).

Beyond the initial transient dynamics the spatial flows exhibit slow oscillations. To compute their time-scale T_p we compute the autocorrelation function of the surface reflectivity in time and locate its first (and strongest) peak. Surprisingly, this time-scale $T_p = 1/f_p$ is much longer than the rotation period of the disks ($1/f$), typically by an order of 10. As the driving frequency increases, the time-scale T_p decreases monotonically for a given viscoelastic fluid. We attribute this slow oscillation of flow to the viscoelasticity of the fluid. It is thus natural to make T_p dimensionless by nor-

malizing it by the relaxation time τ . In Fig. 4, we plot the normalized oscillation frequency of the flow pattern $f_p \tau$ against the Weissenberg number Wi . We observe that for the two different polymer concentrations, and for differing forcing geometries (determined by disk size r and fluid depth h), all the experimental data collapse onto a single curve. This suggests that the oscillation rate of the flow pattern is governed solely by Wi . As shown in Fig. 4 (inset), the flow starts to oscillate only when Wi is above a small threshold, $Wi \gtrsim 0.2$. The solid lines are drawn from a fitting function $f_p \tau = 0.13\sqrt{Wi - 0.2}$, suggesting a supercritical bifurcation from a laminar state to oscillation.

Detailed dynamics of the fluid cells depends sensitively on the Weissenberg number. Fig. 5 illustrates how Wi demarcates different dynamical behaviors. At extremely slow driving ($Wi \ll 1$), the fluid approaches the Newtonian limit. The corresponding flow is steady, with the cells aligning well with the forcing lattice (Fig. 5a) and the deformation of the free surface relatively small. When $\dot{\epsilon}_c$ is comparable to τ^{-1} ($Wi \sim 1$), fluid cells oscillate in a regular fashion. In particular, over one half of an oscillation period the cellular flow pattern evolves to a nearly identical image except having reversed left–right (or up–down) symmetry (Fig. 5b and b'). The oscillation period matches the time-scale T_p obtained from the autocorrelation analysis. With $\dot{\epsilon}_c$ further increased ($Wi \sim 10$), the periodic oscillations disappear, the fluid cells differentiate in size and oscillate irregularly. The flow is quite agitated and has expanding cells that may merge with their neighbors, while shrinking cells may eventually vanish (Fig. 5c). Moreover, the now-roiling fluid cells are no longer easily identified with the forcing lattice.

PIV measurements near the fluid surface illustrate how the flow field reflects the dynamics of the surface morphology. The PIV measurements are performed at $\Delta H = 1$ mm below the free surface. To set up the PIV measurement, a horizontal light sheet is illuminated from the side by a continuous laser (800 mW, $\lambda = 532$ nm) through a cylindrical lens, aligned 1 mm below the free surface. The thickness of the light sheet is measured to be $d = 0.55 \pm 0.05$ mm. Polyamide particles of 50 μm in diameter (Dantec Dynamics) are used as seeding particles. The images of particles are viewed directly from an overhead high-speed camera, as shown in Fig. 1.

The deformed free surface can cause error in the PIV measurements due to refraction: a fluid dome acts like a lens and shifts the location of any tracing particle. However, the deformation of

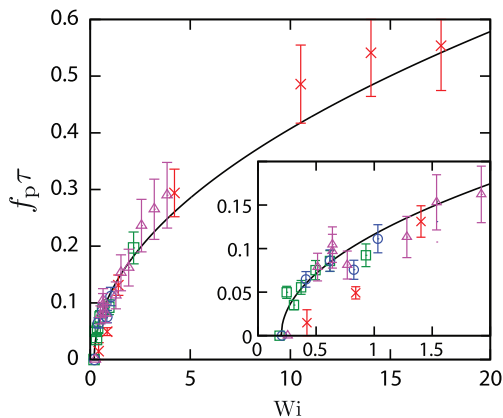


Fig. 4. The oscillation frequency of the flow pattern, $f_p = 1/T_p$, normalized by the fluid relaxation time τ as a function of Wi . This data set is for different disk radii r , fluid depths h , and polymer concentrations c : \times , $r = 6.4$ mm, $h = 11$ mm, $c = 200$ ppm; \square , $r = 3.2$ mm, $h = 5$ mm, $c = 200$ ppm; \circ , $r = 3.2$ mm, $h = 11$ mm, $c = 200$ ppm; \triangle , $r = 6.4$ mm, $h = 11$ mm, $c = 40$ ppm. The inset shows a zoomed-in view near the origin. Flow patterns start to oscillate ($f_p > 0$) when $Wi \gtrsim 0.2$. Solid lines are drawn from the same function $f_p \tau = 0.13\sqrt{Wi - 0.2}$ and shown at different scales.

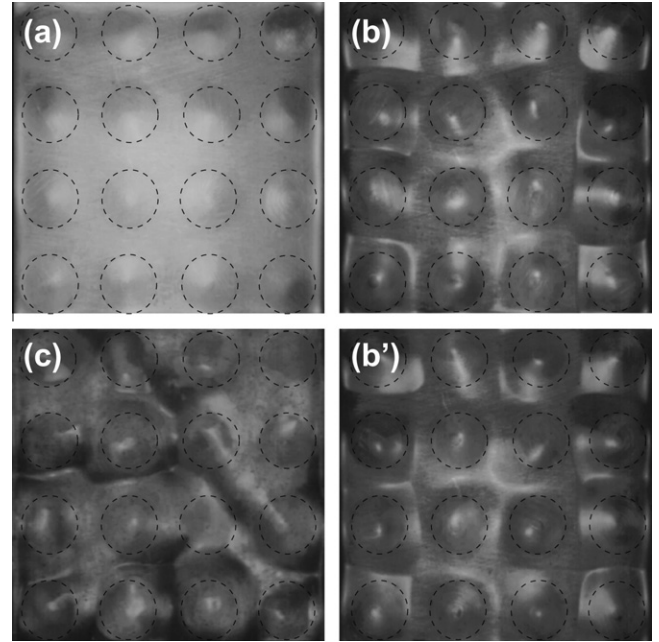


Fig. 5. Dependence of the surface morphologies on the Weissenberg number Wi . (a) At low Wi ($Wi = 0.22$) fluid cells are aligned with the forcing lattice. (b and b') At intermediate Wi ($Wi = 1.6$) fluid cells become distorted, and oscillate slowly between (b) and (b') patterns that have left–right (or up–down) symmetries reversed. (c) At yet higher Wi ($Wi = 9.7$) the individual fluid cells are less distinguishable and fluctuate in location and in size.

the free surface is typically small in our experiments, up to $\Delta H = 1$ mm in height over a 20 mm horizontal span. Assuming a perfect-dome geometry, its radius R is about 50 mm. Using the paraxial lens equation $l' - l = (n - 1)\Delta H l / (nR)$, where n is the refraction index of the fluid, l and l' are the real and apparent offsets of the tracing particle measured from the dome center, respectively. Thus the quantity $l' - l$ is the distortion of the particle position measurement caused by refraction. When close to the worst situation where the fluid surface is most deformed, our estimate gives $l' - l < 0.05$ mm, given that $l = 10$ mm and $R = 50$ mm ($\Delta H \sim 1$ mm). The maximum distortion is thus comparable to the particle size, which is about 0.05 mm in diameter. The error of PIV measurements due to surface distortion is thus negligible within our experimental regime.

Fig. 6 shows the resolved flow field above the middle four disks, at three different values of Wi close to those used in Fig. 5. When the strain rate is low ($Wi \ll 1$) the flow field is steady, and as is consistent with the surface morphology shown in Fig. 5, the flow can be divided into square fluid cells (Fig. 6a). A stagnation point is located at the intersection of any 4 neighboring cells. When the strain rate is sufficiently high ($Wi \sim 1$), the flow pattern is distorted from the square lattice, though with the stagnation point still close to its original location (Fig. 6b and b'). The flow pattern is also no longer steady but shows regular oscillations. Fig. 6b and b' are two snapshots of the resolved flow field, taken half a period apart (typically ~ 10 s). During each period, two vortices of the same sign (e.g., blue¹ vortices in Fig. 6b) move close to each other while the other two (red vortices) are pushed away from the stagnation point. The two vortices that move apart will eventually move back and take over the center position (Fig. 6b'). As Wi further increases the regularity of the flow breaks down and the flow becomes unpinning from the forcing geometry (Fig. 6c). The flows that emerge are also larger than the scale of the forcing lattice.

¹ For interpretation of color in Figs. 1–4, 6, and 7 the reader is referred to the web version of this article.

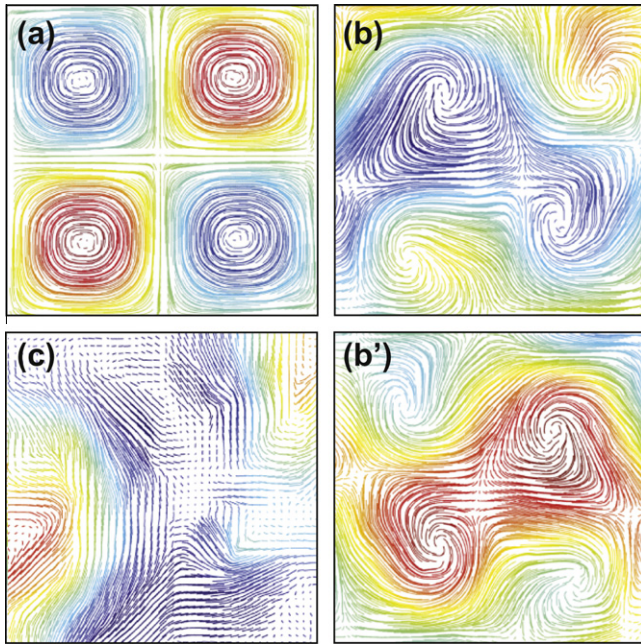


Fig. 6. Typical flow fields of the viscoelastic fluid above the middle 4 disks at different Weissenberg numbers Wi . Stream lines are obtained through PIV measurement. The 2D stream function ψ of the corresponding flows, obtained by solving $\nabla^2\psi = \omega$ where ω is the scalar vorticity of the quasi-2D flow, is shown in color. (a) At low Wi ($Wi = 0.22$) the flow pattern is nearly Newtonian with counter-rotating vortices each centered above a disk. (b and b') When Wi is sufficiently high ($Wi = 1.28$) the strength and the position of the vortices fluctuates periodically. Snapshots (b) and (b') are half a period apart. (c) At even higher Wi ($Wi = 8.42$) the flow field no longer follows the forcing lattice and fluctuates stochastically in space and time.

The PIV measurements allow quantitative analysis of the flow field. Fig. 7 shows the temporal dependencies of flow velocities in different Weissenberg number regimes. As shown in Fig. 7a, the two components (u , v) of the in-plane flow velocities \vec{V} are sampled at the same location near the free surface (shown by the dark dot in the inset of Fig. 7b). The local velocities are normalized by $2\pi f_0 r$, the linear speed of the disks that rotate at frequency f_0 . Fig. 7b shows the spectra of the u component of the local velocity. It should be noted that very similar spectra are also observed for v (not shown). In the Newtonian case ($Wi = 0$), the local velocity is steady. The temporal independence of the flow is further confirmed by the spectra of $u(t)$ (dotted curve in Fig. 7b).

As the flow starts to oscillate at increased Wi ($Wi \sim 1$), the magnitude of the local velocity decreases as compared to the Newtonian case. The two components of the local velocity (u and v) oscillate at the same frequency. The flow are surprisingly periodic despite the fact that the oscillation is spontaneous. The spectrum of u shows a typical periodic oscillation, where there is a peak at a low frequency f_p as compared to the driving frequency f_0 , with the higher order harmonics clearly visible, as shown in solid dark curve in Fig. 7b. For even higher Wi (e.g., $Wi \sim 10$), the magnitude of the local velocity further decreases (Fig. 7a). As shown by its spectrum (solid gray curve in Fig. 7b), the oscillation of the local velocity is composed of multiple modes at various frequencies, which contribute to the irregular oscillation state of the fluid cells in the high Wi regime.

4. Discussion

We have demonstrated that a fluid can exhibit complex nonlinear dynamics, even in the absence of fluid inertia, when viscoelas-

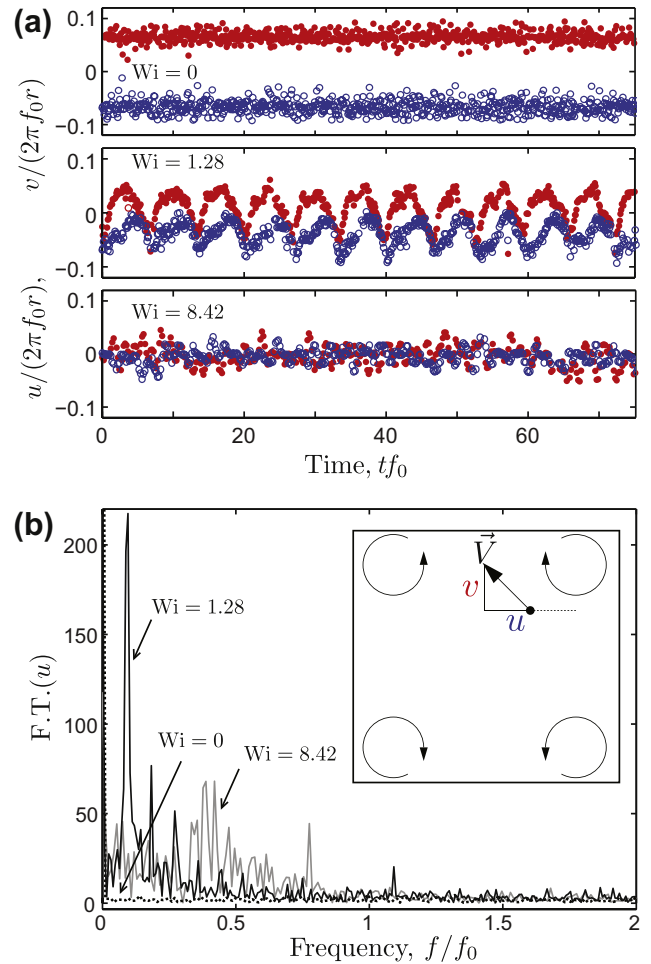


Fig. 7. Temporal behavior of a point velocity in the flow at various Wi . (a) An in-plane velocity \vec{V} at a fixed point as a function of time t near the free surface at different Weissenberg numbers Wi . This point is arbitrarily chosen and marked by a dark dot in the inset of (b), where the circling arrows show the directions of the underlying rotating disks. Time t is normalized by the rotation frequency of the disks f_0 , while the two components of the in-plane velocity, u and v (presented with symbol \circ and \bullet respectively) are normalized by the characteristic linear speed of the rotating disks $2\pi f_0 r$. For a Newtonian fluid ($Wi = 0$) flow is steady. At an intermediate Wi ($Wi \sim 1$) the flow shows regular oscillations. As Wi increases ($Wi \sim 10$) the flow speed further decreases with the periodicity of the oscillating flow destroyed. (b) The Fourier transform of u with respect to time. With increasing Wi ($Wi = 0, 1.28, \text{ and } 8.42$), the distinctly different spectra show that the flow transforms from steady state to a periodic oscillation, and thence to a multi-frequency oscillating (or chaotic) state.

ticity plays a role. This is consistent with previous experiments that used rotational shearing or driven flow through wavy channels [2,3]. Here the nonlinear dynamics arises through a transition from steady flows very similar to the Newtonian case, to regularly oscillating flows, and thence to roiling flows, as the Weissenberg number is systematically increased.

There are points of similarity and difference with the numerical studies of Thomases et al. [10,11] who used a geometrically similar forcing to drive dynamics in a two-dimensional viscoelastic fluid modeled by the Oldroyd-B equations. Both this study and theirs show the appearance of oscillations that are slow relative to the driving period. However, in their study the transition to oscillations was from a broken-symmetry steady-state which we do not observe here but which was observed in other experiments et al. [8,9]. Further, the transition to oscillations here occurs at a much lower Weissenberg number than the transitions observed in Thomases et al. The complex flows at high Wi regime do resemble the multi-frequency state observed in the numerical simulations,

where the fluid cells are delocalized from the forcing background with the flow velocity frequently altering its directions [10,11]. Unlike the simulations, our experiment drives the fluid by a set of disks rotating at constant angular velocity instead of through application of a constant body force. The stresses applied by the disks depend on the flow field that they generate, which forms a feedback loop. It is plausible that this feedback mechanism contributes to the periodic oscillation of the flow at the intermediate Wi regime. Again, this observation is significantly different from that of steady flows with asymmetry observed in simulations [19,10] and in other micro-fluidic experiments [8,9]. In our experiment, this oscillating flow at the intermediate Wi regime could be applied for controlled mixing when fluid inertia is negligible (see [11] for a numerical analysis of mixing flows found in this state). Moreover, the use of a sixteen-roll-mill (instead of a four-roll-mill) can produce richer dynamics and enhanced mixing, as observed in recent simulations [20]. Thus, the difference in lattice geometry will also contribute to the observed differences between experiments and simulations with a four-roll-mill.

Although the time-scale of the oscillation of fluid cells is apparently set by the Weissenberg number Wi , it is likely that the amplitude of the oscillation is sensitive to other viscoelastic parameters, such as the ratio of the polymer viscosity to the solvent viscosity η_p/η_s . Exploring these dependencies is the subject of future study.

Acknowledgements

We thank Anke Lindner and Becca Thomases for helpful discussions. This work is partially supported by NSF Grants DMS-

0652775 (FRG), MRI-0821520 and DMR-0820341 (NYU MRSEC) and the DOE Grant DE-FG02-88ER25053.

References

- [1] R.G. Larson, E.S.G. Shaqfeh, S.J. Muller, *J. Fluid Mech.* 218 (1990) 573.
- [2] A. Groisman, V. Steinberg, *Nature* 405 (2000) 53.
- [3] A. Groisman, V. Steinberg, *Nature* 410 (2001) 905.
- [4] T.T. Perkins, D.E. Smith, R.G. Larson, S. Chu, *Science* 268 (1995) 83.
- [5] P.G. De Gennes, *J. Chem. Phys.* 60 (1974) 5030.
- [6] E.J. Hinch, in: *Polymeres et Lubrification Colloques Internationaux du C.N.R.S.*, vol. 233, Editions du CNRS, Paris, 1974, p. 241.
- [7] A. Groisman, M. Enzelberger, S.R. Quake, *Science* 300 (2003) 955.
- [8] L.E. Rodd, T.P. Scott, D.V. Boger, J.J. Cooper-White, G.H. McKinley, *J. Non-Newton. Fluid Mech.* 129 (2005) 1.
- [9] P.E. Arratia, C.C. Thomas, J. Diorio, J.P. Gollub, *Phys. Rev. Lett.* 96 (2006) 144502.
- [10] B. Thomases, M. Shelley, *Phys. Rev. Lett.* 103 (2009) 094501 (see [20] for the simulation of a viscoelastic flow under a “sixteen-roll-mill” forcing).
- [11] B. Thomases, M. Shelley, J.-L. Thiffeault, *Physica D* 240 (2011) 1602.
- [12] S. Berti, G. Boffetta, *Phys. Rev. E* 82 (2010) 036314.
- [13] D.V. Boger, *J. Non-Newton. Fluid Mech.* 3 (1977) 87.
- [14] A. Groisman, V. Steinberg, *Phys. Rev. Lett.* 77 (1996) 1480.
- [15] G. Prilutski, R.K. Gupta, T. Sridhar, M.E. Ryan, *J. Non-Newton. Fluid Mech.* 12 (1983) 233.
- [16] R.B. Bird, R.C. Armstrong, O. Hassager, *Dynamics of Polymeric Liquids: Fluid Mechanics*, 2 ed., Wiley, 1987.
- [17] J. Serrin, *Angew. Math. Mech.* 39 (1959) 295.
- [18] B.D. Coleman, H. Markovitz, W. Noll, *Viscometric Flows of Non-Newtonian Fluids*, Springer-Verlag, Berlin, 1966.
- [19] R.J. Poole, M.A. Alves, P.J. Oliveira, *Phys. Rev. Lett.* 99 (2007) 164503.
- [20] B. Thomases, unpublished.